An Iron Pyridyl-Carbene Catalyst for Low Overpotential CO_2 reduction to CO: Mechanistic Comparisons with the Ruthenium Analogue and Photochemical Promotion

Sergio Gonell,[a,b,*] Julio Lloret-Fillol,[b,c,*] and Alexander J. M. Miller[a,*]

[a] University of North Carolina at Chapel Hill, Chapel Hill, NC 27599-3290 United States

[b] Institute of Chemical Research of Catalonia (ICIQ), The Barcelona Institute of Science and Technology, Avinguda Països Catalans 16, 43007 Tarragona, Spain

[c] Catalan Institution for Research and Advanced Studies (ICREA), Passeig Lluïs Companys, 23, 08010 Barcelona, Spain

Corresponding Author E-mail Addresses:

sgonell@iciq.es (S.G.)

jlloret@iciq.es (J.L.)

ajmm@email.unc.edu (A.J.M.M.)

Abstract

Electrocatalysts for CO_2 reduction based on first row transition metal ions have attracted attention as abundant and affordable candidates for energy conversion applications. We hypothesized that a successful strategy in ruthenium electrocatalyst design, featuring two chelating ligands that can be individually tuned to adjust the overpotential and catalytic activity, could be equally applicable in the analogous iron complexes. New iron complexes supported by a redox-active 2,2':6',2"-terpyridine (tpy) ligand and strong *trans* effect pyridyl-N-heterocyclic carbene ligand (1-methyl-benzimidazol-2-ylidene-3-(2-pyridine)) were synthesized, and these isostructural analogues to leading ruthenium catalysts were also found to be active CO_2 reduction electrocatalysts. Electrochemical and computational studies reveal completely distinct mechanisms for the iron and ruthenium complexes, with hemilability in the iron system enabling electrocatalysis at overpotentials as low as 150 mV (ca. 500 mV lower than the ruthenium analogue). Cyclic voltammetry studies elucidated the mechanism of the net $4e^-/2H^+$ process that occurs within the single reductive feature, with an iron solvento complex undergoing reduction, CO_2 activation, and further reduction to an iron carbonyl. The mechanistic insight guided development of photoelectrocatalytic conditions under a continuous flow of CO_2 that exhibited improved performance, with Faradaic efficiency up to 99%.

TOC Graphic

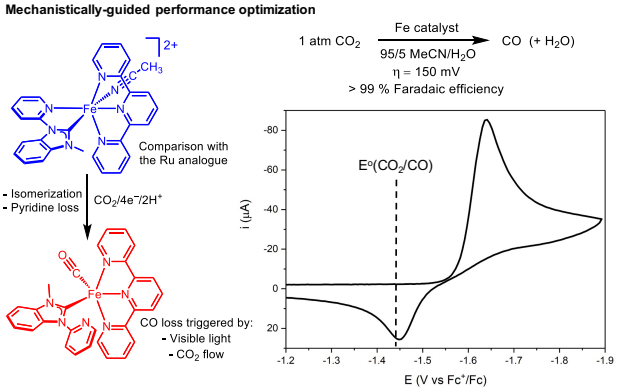

Introduction

Carbon dioxide (CO_2) is an ideal carbon source for the sustainable synthesis of fuels and chemicals. CO_2 utilization by electrochemical reduction holds promise, despite inherent challenges in achieving selective conversion to a particular carbon-containing product (while avoiding H_2 production) with high activity at low overpotential. Molecular electrocatalysts have attracted widespread attention for overcoming some of these challenges to achieve high activity and high selectivity, often through a mechanism-guided development approach.[1,2]

An emerging design motif in molecular electrocatalysts for CO_2 reduction involves pairing a redox-active supporting ligand with a strongly donating, but redox-inactive supporting ligand.[3–5] The prototypical catalysts following this design are ruthenium complexes supported by 2,2':6',2''-terpyridine (tpy) and pyridyl-N-heterocyclic carbene (pyridyl-NHC) ligands. The complex *C-trans*-$[Ru(tpy)(Mebim\text{-}py)(MeCN)]^{2+}$ (Mebim-py = 1-methyl-benzimidazol-2-ylidene-3-(2-pyridine)),[6] where *C-trans* denotes the isomer with the NHC carbon sitting *trans* to the monodentate ligand, can achieve high activity without sacrificing overpotential.

Mechanistic studies of isolated isomeric *C-trans* and *N-trans* (isomer with the N atom of the Mebim-py *trans* to the monodentate ligand) Ru complexes indicate that the high activity is a direct result of the strong *trans* effect of the NHC ligand.[6] This phenomenon,[7] commonly invoked in organometallic chemistry but rarely connected to electrocatalyst performance, can explain the dramatic acceleration of CO ligand dissociation when the strongly σ-donating NHC sits *trans* to the active site. The overpotential is separately controlled by the redox-active tpy ligand in these complexes, leading to a situation where the kinetics of key chemical steps and the reduction potential that initiates electrocatalysis are decoupled.

To date, this approach of independently tunable reduction potentials and chemical kinetics in CO_2 electroreduction has only been explored for ruthenium complexes. Yet we hypothesized

that these design features should be equally applicable to first row transition metal complexes. For example, both Mn[8–10] and Re[11,12] complexes that are supported by redox-active bpy ligands have proven to be active electrocatalysts for CO_2 reduction.

Herein we report the synthesis of new iron complexes supported by tpy and Mebim-py and show that these direct isostructural analogues to a leading Ru catalyst are active and efficient CO_2 reduction electrocatalysts at mild potentials. A single electrochemical feature is observed under CO_2, prompting a mechanistic study that elucidated a rapid $4e^-/2H^+$ transformation from an iron solvento complex to an iron carbonyl. These studies reveal important differences between the isostructural iron and ruthenium catalysts, with rapid ligand substitution kinetics at iron enabling low overpotential electrocatalysis and access to a distinct resting state. The mechanistic insight guided development of photoelectrocatalytic conditions under a constant flow of CO_2 that show improved activity and Faradaic efficiency.

Results and Discussion

The desired iron complex was synthesized by treating $Fe(tpy)Cl_2$[13] with the free NHC Mebim-py (generated *in situ*, see SI for details) at –78 ºC in THF, followed by addition of KPF_6 in MeCN (Scheme 1). Analytically pure dark-red needles were obtained from a concentrated CH_2Cl_2 solution of the complex layered with Et_2O. X-ray diffraction studies confirmed the composition of the product as *C-trans*-$[Fe(tpy)(Mebim\text{-}py)(MeCN)][PF_6]_2$ (***C*-Fe-MeCN^{2+}**, Figure 1), with an octahedral geometry in which the NHC is positioned *trans* to the monodentate ligand, MeCN. The sharp, well-resolved ^{1}H NMR signals of ***C*-Fe-MeCN^{2+}** confirm that the complex is diamagnetic with a low-spin d^6 configuration. The chemical shift of the *N*-methyl resonance is diagnostic of complex geometry in Mebim-py complexes, with the upfield resonance at 2.78 ppm indicating a *C-trans* geometry (Figure S1 in the SI).[6] ^{13}C NMR spectroscopy shows the characteristic resonance of the metallated carbene carbon at 215.9 ppm (Figure S2 in the SI).

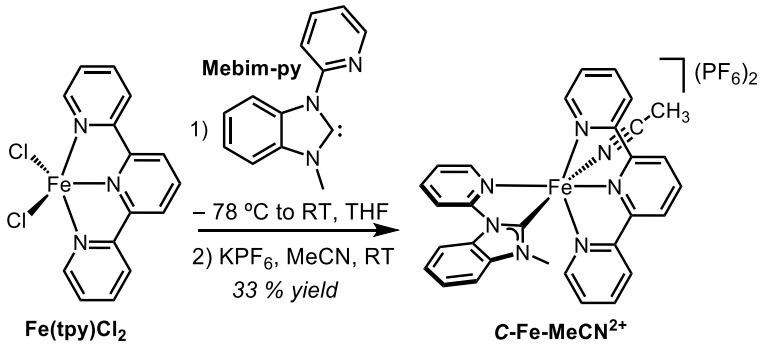

Scheme 1. Synthesis of ***C*-Fe-MeCN^{2+}**.

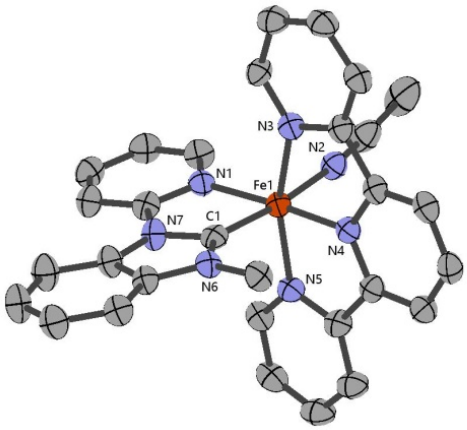

Figure 1. Structural representation of ***C*-Fe-MeCN^{2+}** with ellipsoids drawn at the 50% level. Hydrogen atoms, two PF_6 counterions, and dichloromethane solvent are omitted for clarity. Selected distances (Å) and angles (deg): Fe(1)–C(1) 1.922(5), Fe(1)–N(1) 1.997(4), Fe(1)–N(2) 1.978(4), Fe(1)–N(3) 1.985(4), Fe(1)–N(4) 1.870(4), Fe(1)–N(5) 1.985(4); C(1)–Fe(1)–N(2) 171.79(18), N(4)–Fe(1)–N(1) 176.64(16), N(5)–Fe(1)–N(3) 162.30(16).

The *C-trans* isomer ***C*-Fe-MeCN^{2+}** was the only species detected in spectroscopic studies, with no evidence for formation of the corresponding *N-trans* species. Density functional theory (DFT) computational studies using the B3LYP functional,[14] 6-311+g** basis set, and implicit SMD acetonitrile solvation predicted ***C*-Fe-MeCN^{2+}** to be slightly stable than the ***N*-Fe-MeCN^{2+}** (ΔG^{o} = 0.5 kcal·mol^{-1}; all computations are reported as free energies).

Cyclic voltammograms (CVs) of ***C*-Fe-MeCN^{2+}** under N_2 revealed two reversible features, one oxidation ($E_{1/2}$ = 0.63 V vs. Fc^+/Fc, ΔE_p = 59 mV, Figure S12 and S13 in the SI) and one reduction ($E_{1/2}$ = –1.66 V vs. Fc^+/Fc, Figure 2). The peak current of the reduction feature was twice that of the oxidation wave and the peak-to-peak separation (ΔE_p) was only 42 mV, consistent with a 2e$^-$ process.[10,15] Multi-segment CVs (Figure S14) over a wide range of scan rates showed little variation, as expected for an EEC mechanism involving two electron transfers at the same potential followed by acetonitrile dissociation. DFT computations are also consistent with an EEC mechanism. The ***C*-Fe-MeCN^{2+}/*C*-Fe-MeCN^{+}** reduction potential and the ***C*-Fe-MeCN^{+}/*C*-Fe^{0}** reduction potential (with concurrent acetonitrile dissociation) are computed to occur at the same potential (–1.90 V vs Fc^+/Fc). The singly reduced complex ***C*-Fe-MeCN^{+}** is also predicted to be more stable than the *N-trans* isomer ***N*-Fe-MeCN^{+}**. Further reduction of either species is computationally predicted to produce only a single isomer, *C-trans*-Fe(tpy)(Mebim-py) (***C*-Fe^{0}**): all attempts to optimize an *N-trans* isomer

of the doubly reduced complex resulted in rearrangement to ***C*-Fe^0** in a square pyramidal *C-trans* geometry.

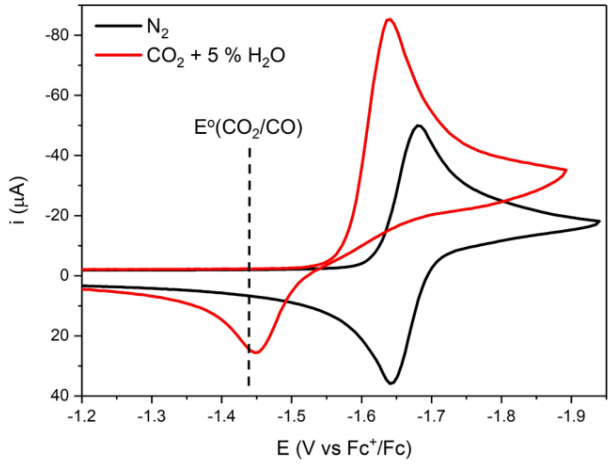

Figure 2. CV of ***C*-Fe-MeCN^{2+}** in MeCN under N_2 atmosphere (black) and under CO_2 atmosphere with 5 % H_2O. Conditions: [Fe] = 1 mM, [$TBAPF_6$] = 100 mM, 3 mm glassy carbon disc working electrode, Pt wire counter electrode, Ag wire pseudo-reference electrode, 100 mV/s.

The initial reduction of ***C*-Fe-MeCN^{2+}** is proposed to be centered on the tpy ligand, based on DFT computations showing the highest occupied molecular orbital (HOMO) of ***C*-Fe-MeCN^{+}** predominantly located on tpy (Figure 3, top and Section 6 in the SI). The similarity of the first reduction potentials of ***C*-Fe-MeCN^{2+}** ($E_{1/2}$ = –1.66 V) and the Ru analogue ***C*-Ru-MeCN^{2+}** ($E_{1/2}$ = –1.69 V)[3,6] provide further evidence for a ligand-centered reduction in each case. The species formed after 2e$^-$ reduction and acetonitrile dissociation, ***C*-Fe^0**, features a HOMO with a high degree of metal character along with some tpy character (Figure 2, bottom). While the HOMO in the analogous Ru complex ***C*-Ru^0** has similar orbital character, it is only accessed at much more negative potentials ($E_{1/2}$ = –1.94 V *vs.* Fc^+/Fc).[3,6] The higher electronegativity and less destabilized d-orbitals in iron complexes can help explain the milder reduction second potential.[16]

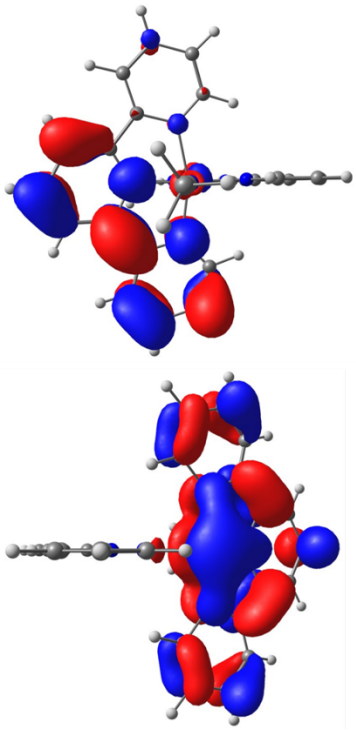

Figure 3. HOMO of ***C*-Fe-MeCN^{+}** (top) and ***C*-Fe^{0}** (bottom).

Water was chosen as the proton source for CO_2 reduction to enable comparisons with the Ru analogues.[6] Under N_2, CVs in 95/5 MeCN/H_2O were essentially identical to those collected in pure MeCN (Figure S15 in the SI). With no indication of metal hydride formation or H_2 evolution catalysis upon reduction of ***C*-Fe-MeCN^{2+}** in the presence of water, there was a clear opportunity for selective reduction of CO_2.

Under 1 atm CO_2, the CVs underwent striking changes. The reduction feature became irreversible, with the cathodic peak potential shifting anodically and the cathodic peak current ($i_{p,c}$) doubling (Figure 2 and Figure S16 in the SI). This behavior is consistent a rapid chemical reaction with CO_2 upon reduction of ***C*-Fe-MeCN^{2+}**, followed by additional electrochemical reactions to give a total of $4e^-$ transferred in the single reduction feature.

Controlled potential electrolysis (CPE) of CO_2-saturated 95/5 MeCN/H_2O solutions of ***C*-Fe-MeCN^{2+}** at −1.68 V vs Fc^+/Fc passed sustained current during 1 h (passing 450 mC of charge at a 3 mm GC working electrode, Scheme 2 and Figure S17 in the SI). The only product detected in the gas phase (by gas chromatography) or liquid phase (NMR and ion chromatography) was CO, produced in 33% Faradaic efficiency (FE). Monitoring the reaction by UV-vis spectroelectrochemistry (SEC) in CO_2-saturated 95/5 MeCN/H_2O revealed the formation of a new species featuring a broad absorption extending beyond 900 nm (Figure S18 in the SI), while infrared SEC revealed the growth of a new strong band at 1831 cm^{-1}

(Figure 4) indicative of a low-valent Fe carbonyl complex. The resting state during electrocatalysis is therefore a low-valent carbonyl complex, providing a plausible explanation for the low FE (which measures gas-phase CO, and does not account for catalyst-bound CO). The new iron complex ***C*-Fe-MeCN^{2+}** thus facilitates the reduction of CO_2 to CO with excellent selectivity relative to H_2 and other carbon-containing products and at only 240 mV overpotential (under the utilized conditions, $E^{o}_{CO2/CO}$ = –1.44 V vs Fc^{+}/Fc).[17]

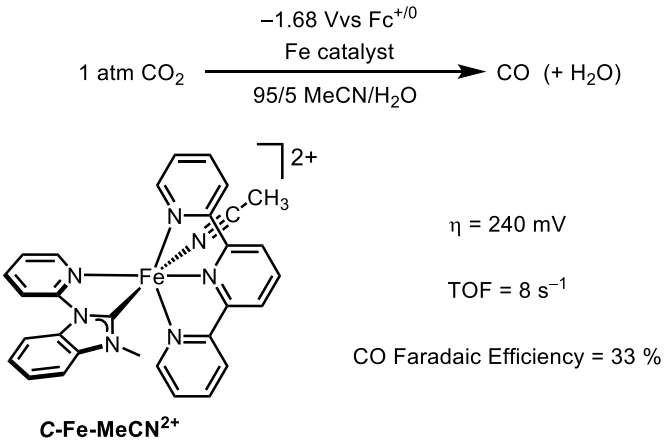

Scheme 2. Catalytic performance of ***C*-Fe-MeCN^{2+}**

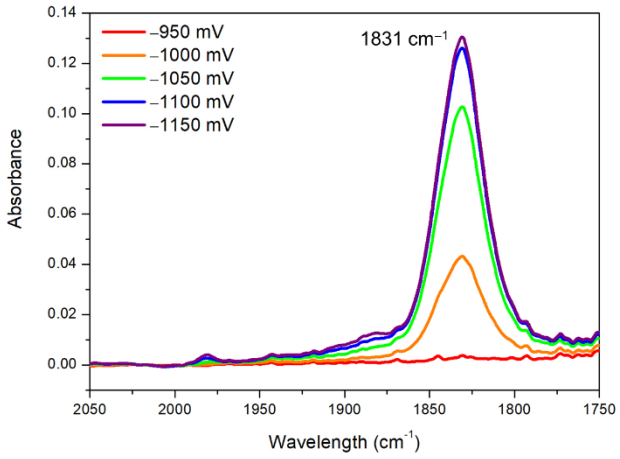

Figure 4. IR-SEC monitoring reduction of ***C*-Fe-MeCN^{2+}** with applied potential (vs. Ag wire pseudoreference) stepped from –950 mV to –1150 mV. Conditions: CO_2 atmosphere, [Fe] = 3 mM, [$TBAPF_6$] = 100 mM, MeCN + 5 % H_2O, Au working electrode, Pt wire counter-electrode, Ag wire pseudo-reference electrode.

A detailed study of the mechanism of CO_2 reduction mediated by ***C*-Fe-MeCN^{2+}** was undertaken, motivated by the very low overpotential, the unusual voltammetric response consistent with a single and rapid $4e^{-}/2H^{+}$ reduction, and the promise of directly comparing

reaction pathways with the previously studied Ru analogue ***C*-Ru-MeCN^{2+}**. A key observation was the appearance of a new reduction feature in multi-segment CVs of solutions of ***C*-Fe-MeCN^{2+}** in 95/5 MeCN/H_2O under 1 atm CO_2 (Figure 5a). This new feature is attributed to the reduction of an intermediate iron complex formed during electrochemical CO_2 reduction. The appearance of a new feature anodic of ***C*-Fe-MeCN^{2+}**, along with the decrease in cathodic peak current ($i_{p,c}$) for the initially observed reduction, is precisely the scenario expected for an ECE-type mechanism, wherein the intermediate is easier to reduce than the initial complex ***C*-Fe-MeCN^{2+}**.[18–22]

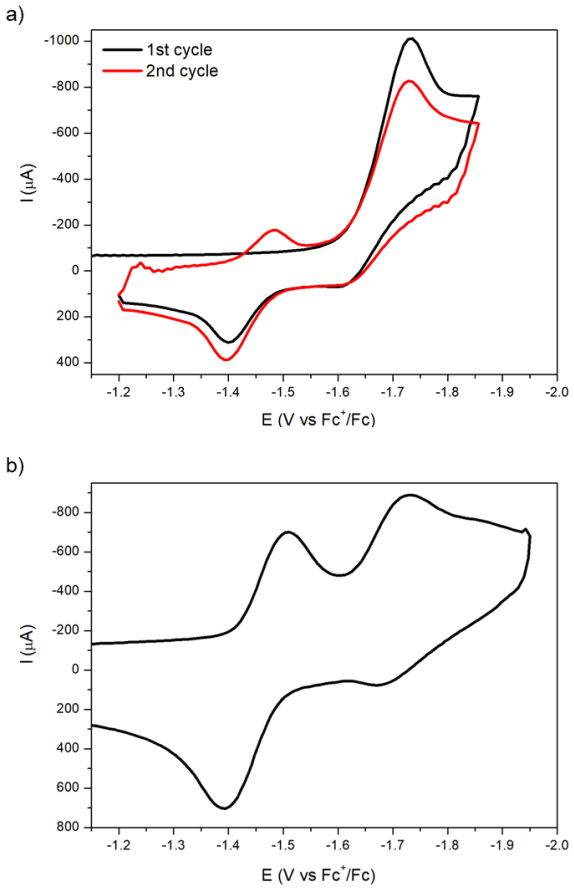

Figure 5. (a) Multi-segment CV of ***C*-Fe-MeCN^{2+}** in MeCN under CO_2 atmosphere with 5 % H_2O. **(**b) CV of ***N*-Fe-CO^{2+}** in MeCN under N_2 atmosphere. Conditions: [Fe] = 1 mM, [$TBAPF_6$] = 100 mM, 3 mm glassy carbon disc working electrode, Pt wire counter electrode, Ag wire pseudo-reference electrode, 40 V/s.

Hypothesizing that the redox-active intermediate detected in CV studies was a carbonyl complex, an iron(II) carbonyl derivative was independently synthesized. Treatment of ***C*-Fe-MeCN^{2+}** with CO in CH_2Cl_2 at room temperature resulted in precipitation of an orange solid. The strong IR band at 2023 cm^{-1} in the isolated product confirmed the presence of a carbonyl

ligand (Scheme 3). The ^{1}H NMR spectrum displays a singlet at 4.77 ppm for the *N*-methyl protons (Figure S4 in the SI), with a far downfield shift relative to ***C*-Fe-MeCN^{2+}** announcing isomerization to an *N-trans* geometry.[6] An X-ray diffraction study confirmed the constitution of *N-trans*-[Fe(tpy)(Mebim-py)(CO)][PF_6]$_2$, ***N*-Fe-CO^{2+}** (Figure 6). The geometric isomerization during ligand substitution was unexpected, considering that the Ru analogue ***C*-Ru-MeCN^{2+}** was readily converted to ***C*-Ru-CO^{2+}** without rearrangement.[6] A plausible mechanism supported by DFT computations involves Mebim-py hemilability (see Section 6 in the SI). Initial MeCN dissociation is followed by a "windshield wiper" rotation that converts the five-coordinate intermediate ***C*-Fe^{2+}** to ***N*-Fe^{2+}** before CO binding produces ***N*-Fe-CO^{2+}** (Figure S39 in the SI). All the complexes bearing a CO ligand showed thermodynamic preference for the *N-trans* geometry.

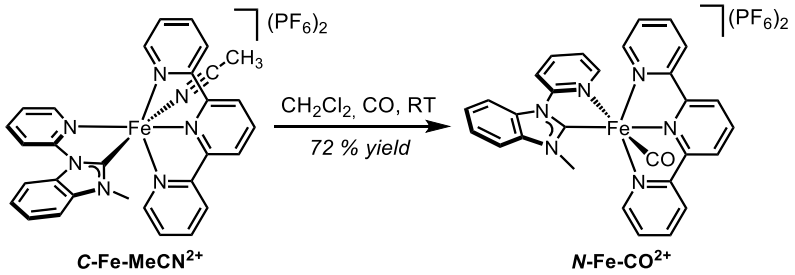

Scheme 3. Synthesis of ***N*-Fe-CO^{2+}**

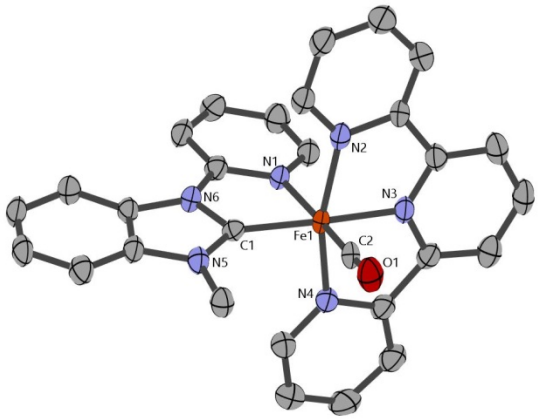

Figure 6. Structural representation of ***N*-Fe-CO^{2+}** with ellipsoids drawn at the 50% level. Hydrogen atoms, two PF_6 counterions, and dichloromethane solvent are omitted for clarity. Selected distances (Å) and angles (deg): Fe(1)–C(1) 1.921(5), Fe(1)–N(1) 2.015(4), Fe(1)–N(2) 1.991(4), Fe(1)–N(3) 1.919(4), Fe(1)–N(4) 1.979(4), Fe(1)–C(2) 1.774(5), C(2)–O(1) 1.144(6); C(1)–Fe(1)–N(3) 172.64(18), N(1)–Fe(1)–C(2) 173.30(19), N(2)–Fe(1)–N(4) 161.43(17).

CVs of ***N*-Fe-CO^{2+}** at 40 V/s reveal an initial reduction with a very similar $E_{p,c}$ value to the feature observed in multi-segment CVs of ***C*-Fe-MeCN^{2+}** under CO_2, and a return oxidation that also aligns almost perfectly with the oxidation feature in catalytic conditions (Figure 5b). While the details of the reduction of ***N*-Fe-CO^{2+}** will be examined later, these comparative CVs clearly pointed to the intermediacy of ***N*-Fe-CO^{2+}** during catalysis.

The reduction of ***N*-Fe-CO^{2+}** was monitored in SEC experiments. Applying progressively more negative potentials in an IR-SEC study of ***N*-Fe-CO^{2+}** under N_2 led to the disappearance of the band associated with the starting complex (2023 cm^{-1}), before eventually reaching potentials at which the characteristic 1831 cm^{-1} stretch of the catalytic intermediate appeared (Figure 7). UV-vis-SEC experiments also confirm that reduction of ***N*-Fe-CO^{2+}** forms the species present during catalysis (Figure S19 in the SI).

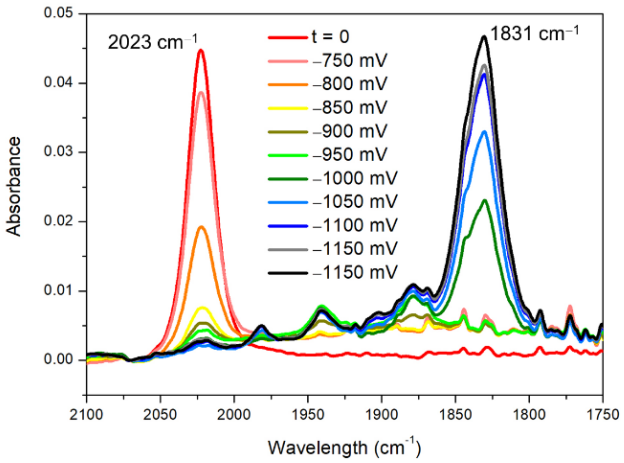

Figure 7. IR-SEC monitoring reduction of ***N*-Fe-CO^{2+}** with applied potentials (vs. Ag wire pseudoreference) from –750 mV to –1150 mV. Conditions: N_2 atmosphere, [Fe] = 3 mM, [$TBAPF_6$] = 100 mM, MeCN, Au working electrode, Pt wire counter-electrode, Ag wire pseudo-reference electrode.

To gain additional insight into the structure of the low-valent Fe carbonyl species, an authentic synthesis was designed. Treating ***N*-Fe-CO^{2+}** with two equivalents of Cp^*_2Co ($E^{o'}$ = –1.91 V *vs.* Fc^+/Fc)[23] in THF-d_8 led to a color change from pale orange to dark red. The resulting ^1H NMR spectrum revealed clean conversion to a single new diamagnetic species (Figure S7 in the SI). The $^{13}C\{^1H\}$ NMR spectrum confirmed the presence of a carbonyl ligand and a metallated carbene carbon (Figure S8 in the SI). The pyridine resonances in the ^1H NMR spectrum have distinct chemical shifts compared to the other complexes in the

family, and these resonances were quite broad at room temperature. On the basis of the combined spectroscopic data, the structure is assigned as a five-coordinate neutral carbonyl complex in which the Mebim-py ligand is bound in a monodentate fashion through the NHC carbon (with the pyridine arm dissociated, Scheme 4). Variable temperature NMR studies are consistent with a fluxional process involving the free pyridyl arm, such as rotation about the M–C_{NHC} bond, with two energetically similar conformers observed at low temperatures (Figures S9 and S10 in the SI).

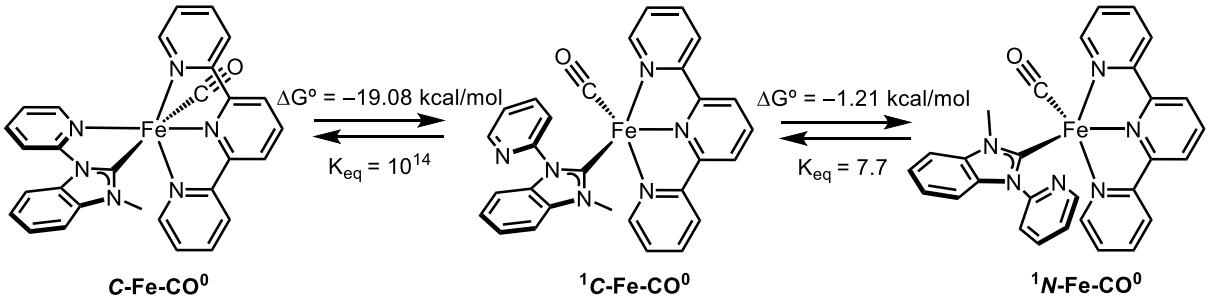

Scheme 4. Relative energy (298 K) differences between doubly-reduced carbonyl complexes.

DFT computations support the proposed structure and conformational dynamics. Efforts to find an energy minimum for the six-coordinate neutral carbonyl complex ***N*-Fe-CO^0** were unsuccessful, with the computations always providing 5-coordinate structures. Two energetically similar conformational isomers with trigonal bipyramidal geometries were optimized, differing in the position of the dangling pyridine group (isomerization $\Delta G = -1.21$ kcal/mol, Scheme 4). The computed IR stretches (1816 cm^{-1} for **κ^1*N*-Fe-CO^0** and 1830 cm^{-1} for **κ^1*C*-Fe-CO^0**) are very similar to the band observed experimentally (1831 cm^{-1}). The six-coordinate isomer ***C*-Fe-CO^0** has a computed CO stretching frequency of 1963 cm^{-1}, and is predicted to be almost 20 kcal/mol higher in energy than the five-coordinate isomers (Scheme 4).

The combined experimental and computational data point to a CO_2 electroreduction mechanism involving 2e$^-$ reduction of ***C*-Fe-MeCN^{2+}** followed by nucleophilic attack of CO_2 and hydrolysis to produce the carbonyl complex of *opposite geometry* ***N*-Fe-CO^{2+}** (Scheme 5). The carbonyl complex is easier to reduce than the original acetonitrile complex, leading to another 2e$^-$ reduction to form a low-valent five-coordinate iron complex **κ^1-Fe-CO^0**. This sequence is noteworthy for the extremely rapid ligand dissociation and isomerization events, which may contribute to the ability to access CO at mild applied potentials. The hemilability

of pyridine is also a defining feature, leading to a stable 18-electron carbonyl species that may inhibit CO release during catalysis.

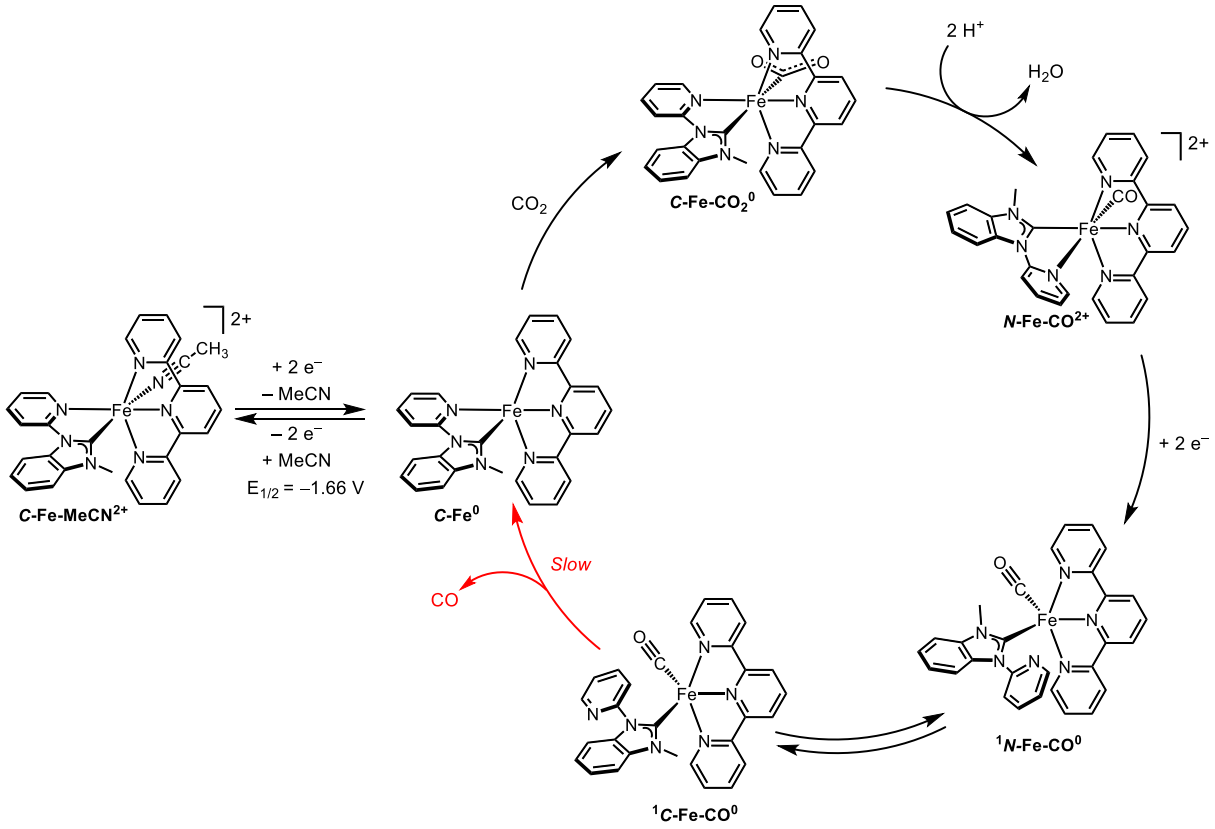

Scheme 5. Proposed mechanism of CO_2 electroreduction starting from ***C*-Fe-MeCN^{2+}**.

To further probe the remarkable $4e^-/2H^+$ transformation that converts CO_2 to CO, the elementary steps involved in the reduction of ***N*-Fe-CO^{2+}** were examined in a series of scan rate dependence cyclic voltammetry studies. The following conditions were compared: (a) ***C*-Fe-MeCN^{2+}** under N_2, (b) ***C*-Fe-MeCN^{2+}** under CO, (c) ***N*-Fe-CO^{2+}** under N_2, and (d) ***N*-Fe-CO^{2+}** under CO. Distinct behavior was observed at fast scan rates (above 1 V/s, Figure 8) and slow scan rates (0.05 to 1 V/s, Figure 9), reflecting the interplay of several chemical and electrochemical steps.

CVs in the fast scan rate regime (between 2 and 30 V/s) are shown in Figure 8. The acetonitrile complex ***C*-Fe-MeCN^{2+}** exhibits a reduction event that has the same scan rate dependent cathodic peak potential under either N_2 or CO (Figure 8a, 8b and S20 in the SI), which suggests that CO binding is not involved (with acetonitrile dissociation presumably limiting the chemical kinetics). Whereas the $2e^-$ reduction is completely reversible under N_2, the CV becomes irreversible under CO. On the basis of the location of the return oxidation,

we assign the process as $2e^-$ reduction followed by CO binding and pyridine loss to give **κ^1-Fe-CO^0**, which is reoxidized to ***N*-Fe-CO^{2+}** during the return sweep. This process was confirmed by multi-segment CVs of solutions of ***C*-Fe-MeCN^{2+}** under 1 atm CO (Figure S21 in the SI, compare it with Figure 5), which revealed the presence of a new reduction feature attributed to the reduction of ***N*-Fe-CO^{2+}** generated at the surroundings of the electrode.

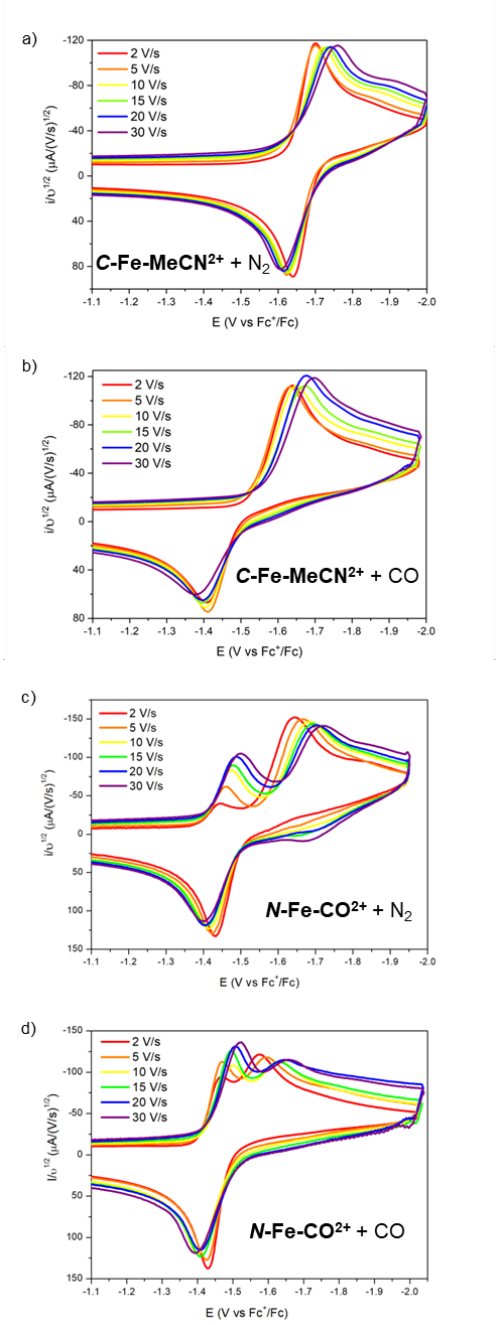

Figure 8. Normalized CVs of ***C*-Fe-MeCN^{2+}** under N_2 atmosphere (a) and under CO atmosphere (b) and of ***N*-Fe-CO^{2+}** under N_2 atmosphere (c) and under CO atmosphere (d) from 2 to 30 V/s. Conditions: N_2, [Fe] = 1 mM, [$TBAPF_6$] = 100 mM, MeCN, GC working disc electrode (3 mm), Pt wire counter-electrode, Ag wire pseudo-reference electrode.

CVs of ***N*-Fe-CO^{2+}** under N_2 above 1 V/s display two reduction waves in the forward scan and two oxidation features in the return sweep, suggesting two reversible reduction events (Figure 8c and S22 in the SI). The first reduction is anodically shifted relative to ***C*-Fe-MeCN^{2+}** by about 200 mV, as is typical for carbonyl complexes.[6] Reversing the sweep such that only the first feature is present gives a peak-to-peak separation consistent with a $1e^-$ reduction (Figure S23 in the SI). The second reduction appears at the almost the same potential as seen for ***C*-Fe-MeCN^{2+}** under N_2 (Figure 8a). CVs of ***N*-Fe-CO^{2+}** under CO above 1 V/s are qualitatively similar to those under N_2, but the second reduction feature exhibits a substantial anodic shift at all scan rates under CO (Figure 8d). The CO-dependent potential of the second reduction indicates that CO binding is kinetically relevant to the electrochemical response. This situation contrasts the behavior of ***C*-Fe-MeCN^{2+}** under N_2 and CO, suggesting that despite similar potentials, the second reduction feature in Figures 8c and 8d is not simply reduction of ***C*-Fe-MeCN^{2+}**. Instead, the data suggest a reaction sequence in which $1e^-$ reduction of ***N*-Fe-CO^{2+}** is followed by CO dissociation and isomerization to form ***C*-Fe-MeCN^{+}**, which then undergoes $1e^-$ reduction at more negative potentials. ***C*-Fe-MeCN^{+}** and ***C*-Fe-MeCN^{2+}** have almost the same $E_{1/2}$ values, as discussed earlier, but distinct dependence on CO pressure and scan rate. The broader features in CVs of ***N*-Fe-CO^{2+}** under N_2 are attributed to partial CO dissociation, as reflected in the small return oxidation associated with oxidation of ***C*-Fe^{0}** to ***C*-Fe-MeCN^{2+}** (Figures 8c and S22 in the SI).

CVs in the slow scan rate regime are shown in Figure 9. The voltammograms are remarkably different from those collected at fast scan rates. In CVs of ***N*-Fe-CO^{2+}** under N_2 (Figure 9c), the first reduction feature is essentially absent, having decreased into the baseline. Instead, the CV looks quite similar to that of ***C*-Fe-MeCN^{2+}** under CO (Figure 9b). The disappearance of the first reduction wave is attributed to a chemical redox-catalyzed ligand substitution process that consumes ***N*-Fe-CO^{2+}**. The initial reduction product ***N*-Fe-CO^{+}** dissociates CO and isomerizes to form ***C*-Fe-MeCN^{+}**, which reduces another equivalent of ***N*-Fe-CO^{2+}**, initiating a chain reaction that converts all of ***N*-Fe-CO^{2+}** to ***C*-Fe-MeCN^{2+}** while only passing tiny amounts of current. Such electron-transfer chain catalysis is well known in other contexts, including a Re CO_2 reduction catalyst [24–26]

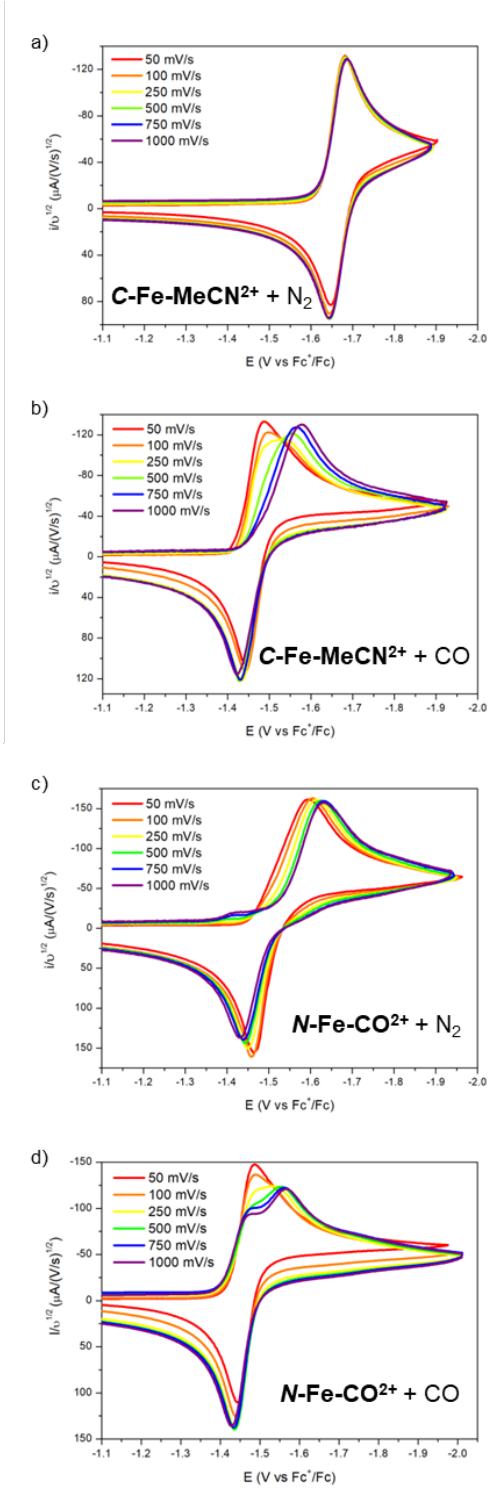

Figure 9. Normalized CVs of ***C*-Fe-MeCN^{2+}** under N_2 atmosphere (a) and under CO atmosphere (b) and of ***N*-Fe-CO^{2+}** under N_2 atmosphere (c) and under CO atmosphere (d) from 0.05 to 1 V/s. Conditions: N_2, [Fe] = 1 mM, [$TBAPF_6$] = 100 mM, MeCN, GC working disc electrode (3 mm), Pt wire counter-electrode, Ag wire pseudo-reference electrode.

The viability of a redox catalysis mechanism of ligand substitution was probed by treating ***N*-Fe-CO^{2+}** with a catalytic amount of the chemical reductant Cp^*_2Co in CD_3CN. Upon addition

of Cp^*_2Co, the solution immediately changed color from pale orange to dark red, and the ^1H NMR spectrum revealed complete conversion of ***N*-Fe-CO^{2+}** to ***C*-Fe-MeCN^{2+}** (Figure S11 in the SI). IR-SEC experiments provide further support for redox catalytic CO release. Holding the potential of the cell only capable of effecting the first reduction process (–820 mV vs. Ag wire pseudoreference) led to the disappearance of the CO stretch of ***N*-Fe-CO^{2+}** without the appearance of a new stretch (Figure S24 in the SI), attributed to loss of redox-catalyzed loss of CO and formation of ***C*-Fe-MeCN^{2+}**. Applying more negative potentials, capable of reducing the newly formed solvento complex (–950 mV vs. Ag pseudoreference) led to the appearance of the band corresponding to the low valent iron carbonyl species.

Under CO, CVs of ***N*-Fe-CO^{2+}** show two features at 1 V/s (Figure 9d), which merge into a single wave as the scan rate is decreased to 50 mV/s. This behavior is attributed to somewhat slower CO dissociation inhibiting the redox catalysis, in conjunction with a significant anodic shift in the reduction of the generated ***C*-Fe-MeCN^{2+}** under CO in this scan rate range. Thus, the reduction feature of ***C*-Fe-MeCN^{2+}** shifts anodically with decreasing scan rates until it is overlapping with the reduction feature of ***N*-Fe-CO^{2+}**. The same anodic shift is also apparent in CVs of ***C*-Fe-MeCN^{2+}** itself under CO (Figure 9b).

A unified mechanism for reduction of the carbonyl complex that is consistent with both the slow and fast scan rate regimes is shown in Scheme 6. The reduction of ***N*-Fe-CO^{2+}** is remarkably complex, featuring CO dissociation and re-association as well as geometric isomerizations. Initial reduction of ***N*-Fe-CO^{2+}** generates ***N*-Fe-CO^{+}**, which undergoes rapid MeCN substitution for the CO ligand and isomerization to generate ***C*-Fe-MeCN^{+}**. At slow scan rates, ***C*-Fe-MeCN^{+}** builds up to sufficient concentrations to initiate a chemical redox-catalyzed substitution process that converts all unreduced ***N*-Fe-CO^{2+}** near the electrode surface to the solvento isomer ***C*-Fe-MeCN^{2+}**. Thus, at slow scan rates, the CVs look essentially identical to those of ***C*-Fe-MeCN^{2+}** itself under N_2. Under 1 atm CO, however, the redox-catalyzed process is somewhat slower. At fast scan rates, the singly-reduced intermediate ***C*-Fe-MeCN^{+}** is electrochemically reduced at a rate that outcompetes the chemical redox-catalyzed substitution reaction. In both cases, CO release is observed initially, but reduction of ***C*-Fe-MeCN^{+}** triggers *re-binding* of CO along with dissociation of the NHC pyridine ligand to form the five-coordinate complex **κ^1-Fe-CO^0**. Whereas ***C*-Fe-MeCN^{2+}** is more stable than ***N*-Fe-CO^{2+}** complex under 1 atm of N_2, while **κ^1-Fe-CO^0** is more stable than ***C*-Fe^0** under 1 atm N_2. The high affinity of **κ^1-Fe-CO^0** for CO helps explain the strong anodic

shifts in the reduction of ***C*-Fe-MeCN^{+}**, which is followed by highly favorable CO association.

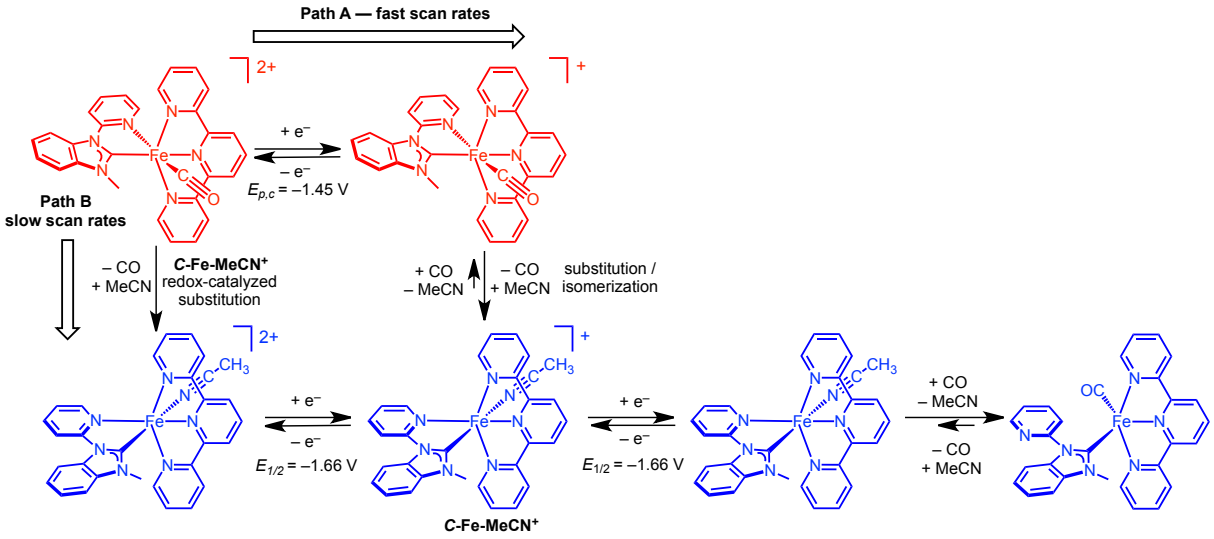

Scheme 6. Competing pathways proposed to operate during reduction of ***N*-Fe-CO^{2+}**.

The mechanistic pathways of Scheme 6 suggest that the pyridine-dissociated complex **κ^{1}-Fe-CO^{0}** has an extraordinarily high CO binding affinity. Even when only one equivalent of CO is present in the system, after dissociation from ***N*-Fe-CO^{2+}**, the stable product **κ^{1}-Fe-CO^{0}** is formed in nearly quantitative yield. We therefore considered CO dissociation from the carbonyl complex **κ^{1}-Fe-CO^{0}** likely to be a limiting process in the overall catalytic process. This is further supported by the observation of this species by IR under during catalysis (*vida supra*).

On the basis of many examples of photochemical CO dissociation,[27–29] we carried out electrocatalysis under simultaneous visible light illumination in an attempt to trigger CO dissociation from **κ^{1}-Fe-CO^{0}**. CVs under illumination slowed a slight current enhancement, indicating increased catalytic activity (Figure S25 in the SI). Bulk electrolysis of ***C*-Fe-MeCN^{2+}** under identical conditions than before (Scheme 2), but under visible light irradiation led to an increase of the Faradaic efficiency for the generation of CO (55 % FE). CO was the only product detected the headspace (by gas chromatography) or in the liquid phase (by NMR). This improvement in the generation of CO leads to a TOF of 14 s^{-1} at an overpotential of just 240 mV.

Electrolysis under a continuous flow of CO_2 was also explored as an alternative strategy for promoting CO release from the low valent iron species, keeping the conditions depicted in Scheme 2. Under applied potentials of –1.68 V vs. Fc^{+}/Fc and with a constant CO_2 flow,

sustained current was passed during more than 1 h (amounting to 7.24 C of charge passed at the GC rod working electrode, Figure S26). As shown in Figure 10, these conditions led to a striking increase in the Faradaic efficiency for the production of CO (average 80%, as compared to only 33% under analogous conditions with a static CO_2 atmosphere).

Conditions of flowing CO_2 open the possibility to reach high efficiencies at low overpotentials. High surface area reticulated vitreous carbon (RVC) was utilized as working electrode for this purpose. Electrocatalytic CO generation was observed at applied potentials as mild as −1.59 V vs Fc^+/Fc, representing an overpotential of only 150 mV.[17] An average Faradaic efficiency of 80% was maintained during the 3 h experiment (Figure S27 and S28 in the SI). The total CO generated in this experiment corresponds to a TON of 10 TON (with respect the total amount of catalyst in solution, representing a gross underestimate due to the large amount of catalyst idling away from the electrode surface at any moment). This overpotential is among the smallest reported to date for a molecular electrocatalyst for CO production.[29–35]

The charge passed during the controlled potential electrolyses under CO_2 flow started to decrease after 1.5 h (Figures S26, S27 and S29), with concomitant decrease in CO generation. The color of the solution change from dark-red to pink, characteristic of the homoleptic complex $[Fe(tpy)_2]^{2+}$.[36] A CV recorded at the end of the experiment revealed two reversible $1e^-$ features (Figure S30 in the SI) at −1.60 V and −1.84 V vs Fc^+/Fc, in close agreement with an authentic sample of $[Fe(tpy)_2]^{2+}$. Long-term stability represents a focus area for future catalyst development.

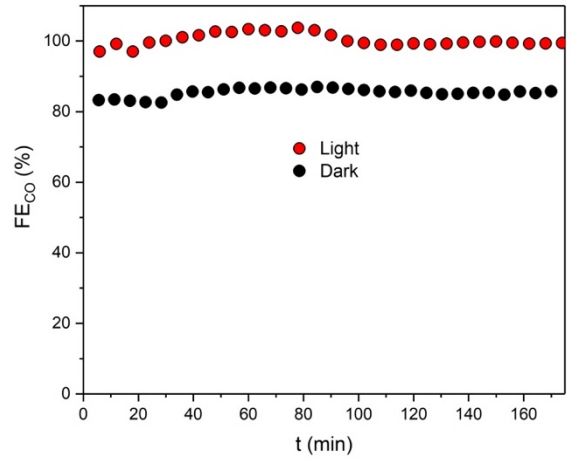

Figure 10. Faradaic efficiency for the generation of CO with respect time, under dark (black dots) and light irradiation (red dots). Conditions: MeCN + 5% H_2O, CO_2 atmosphere, [Fe] = 1 mM, [$TBAPF_6$] = 100 mM, glassy carbon disc working electrode (122.5 mm^2), Pt wire counter

electrode, $Ag/AgNO_3$ reference electrode, applied potential –1.68 V *vs* Fc^+/Fc, constant flow of CO_2 (30 mL/min).

The combination of a constant CO_2 flow and visible light illumination finally provided quantitative Faradaic efficiency. When the working compartment of the cell was irradiated with a mercury arc lamp under a constant flow of CO_2 during electrolysis at –1.68 V vs Fc^+/Fc (Figure S29), CO was produced at an average Faradaic efficiency > 99 % (Figure 10). Comparing the photoelectrochemical conditions of under constant CO_2 flow and under a static atmosphere of CO_2 (Faradaic efficiency >99% and 55%, respectively) reveals the importance of both photodissociation and the mass transport of CO removal.

Conclusions

A new iron complex supported by tpy and pyridyl-carbene ligands was synthesized and found to catalyze electrochemical CO_2 reduction to CO with high selectivity at low overpotentials. Mechanistic studies based on cyclic voltammetry, in situ spectroelectrochemistry, authentic syntheses, and DFT computations elucidate the reaction pathway that completes a $4e^-/2H^+$ reduction of CO_2 to CO in a single voltammetric wave. Each trip through the catalytic cycle involves geometric isomerization between structures with the carbene *trans* to the active site and pyridine trans to the active site. Furthermore, the pyridine connected to the NHC was found to be hemilabile, leading to a relatively stable carbonyl complex. The lability of the pyridine of the Mebim-py ligand, enhanced by the strong trans effect of CO.[7] Recognizing that CO release from the pyridine-dissociated intermediate to be a key step, photoelectrocatalysis was undertaken and found to significantly improve the activity and Faradaic efficiency while maintaining the same selectivity and low overpotential.

Comparisons between the new iron catalyst and the previously studied ruthenium catalyst are instructive.[6] Despite having identical supporting ligands, the behavior between the two systems is strikingly different in most respects. Under N_2, MeCN solutions of ***C*-Ru-MeCN^{2+}** display two sequential $1e^-$ reductions, while ***C*-Fe-MeCN^{2+}** features a single $2e^-$ reduction. The ca. 500 mV difference in the potential of the second reduction results in the iron system having a dramatically lower overpotential for electrocatalytic CO_2 reduction to CO (ca. 150 mV for Fe, ca. 650 mV for Ru). This low overpotential comes at the expense of activity, as the ruthenium system boasts substantially higher rates (ca. 14 s^{-1} for Fe, ca. 2000 s^{-1} for Ru). The difference in activity stems in part from the ruthenium system enjoying turnover free

from CO inhibition (with high activity and Faradaic efficiency under batch conditions in the dark);[3,4,6] the iron system is inhibited by CO, but the use of a constant CO_2 flow and visible light illumination greatly increase efficiency. The mechanistic studies suggest that the differences in activity stem from the dramatically increased ligand lability in the iron system relative to the ruthenium system. During electrocatalysis, ***C*-Ru-MeCN^{2+}** maintains a geometry with the NHC *trans* to the active site, and the pyridine remains bound throughout the cycle. In contrast, ***C*-Fe-MeCN^{2+}** isomerizes to ***N*-Fe-CO^{2+}** rapidly, and upon reduction of this species the pyridine ligand dissociates. This behavior is attributed to the strong *trans* effect of the CO ligand, which in the Ru system is always *trans* to another strong *trans* effect NHC ligand, but in the Fe system lies across from the more labile pyridine ligand. Thus, CO dissociation is extremely rapid in the Ru catalyst, but slow in the Fe catalyst. Nonetheless, illumination and perform the electrolysis under constant flow can promote CO dissociation and accelerate catalysis in the Fe system.

This study shows that Fe and Ru are both viable electrocatalysts supported by tpy and pyridyl-carbene ligands, once the Fe congener can be synthetized. The characteristics of each system are distinct, with different strengths and weaknesses as catalysts. Through careful mechanistic studies, we now understand how ligand lability and isomerization lead to different reaction pathways for Fe relative to Ru. This knowledge will guide the development of new first-row transition metal electrocatalysts.

Supporting information

Experimental details, NMR spectra, electrochemical methods, crystallographic methods, and computational methods (PDF)

Coordinates of computational output files (PDF)

Crystallographic data (CIF)

Acknowledgements

This material is based upon work supported as part of the Alliance for Molecular PhotoElectrode Design for Solar Fuels (AMPED), an Energy Frontier Research Center (EFRC) funded by the U.S. Department of Energy, Office of Science, Office of Basic Energy Sciences under Award Number DE-SC0001011. Quinton J. Bruch and Josh Chen assisted with crystallographic data collection. Brandie M. Ehrmann assisted with mass spectrometry. The mass spectrometry work was supported by the National Science Foundation under Grant No. (CHE-1726291). We would like to thank the European Commission for the ERC-CG-

2014-648304 project and the Spanish Ministry of Science for the project CTQ2016-80038-R (J.Ll.-F). S.G. thanks the EU for Horizon 2020 Marie Skłodowska-Curie Fellowship (grant no.794119, Fe-RedOx-Cat).

References

(1) Francke, R.; Schille, B.; Roemelt, M. *Chem. Rev.* **2018**, *118* (9), 4631.

(2) Gonell, S.; Miller, A. J. M. In *Advances in Organometallic Chemistry*; Perez, P., Ed.; 2018; pp 1–70.

(3) Chen, Z.; Chen, C.; Weinberg, D. R.; Kang, P.; Concepcion, J. J.; Harrison, D. P.; Brookhart, M. S.; Meyer, T. J. *Chem. Commun.* **2011**, *47* (47), 12607.

(4) Chen, Z.; Concepcion, J. J.; Brennaman, M. K.; Kang, P.; Norris, M. R.; Hoertz, P. G.; Meyer, T. J. *Proc. Natl. Acad. Sci. USA* **2012**, *109* (39), 15606.

(5) Kang, P.; Chen, Z.; Nayak, A.; Zhang, S.; Meyer, T. J. *Energy Environ. Sci.* **2014**, *7* (12), 4007.

(6) Gonell, S.; Massey, M. D.; Moseley, I. P.; Schauer, C. K.; Muckerman, J. T.; Miller, A. J. M. *J. Am. Chem. Soc.* **2019**, *141* (16), 6658.

(7) Tsipis, A. C. *Dalton Trans.* **2019**, *48* (5), 1814.

(8) Bourrez, M.; Molton, F.; Chardon-Noblat, S.; Deronzier, A. *Angew. Chem., Int. Ed.* **2011**, *50* (42), 9903.

(9) Smieja, J. M.; Sampson, M. D.; Grice, K. A.; Benson, E. E.; Froehlich, J. D.; Kubiak, C. P. *Inorg. Chem.* **2013**, *52* (5), 2484.

(10) Sampson, M. D.; Nguyen, A. D.; Grice, K. A.; Moore, C. E.; Rheingold, A. L.; Kubiak, C. P. *J. Am. Chem. Soc.* **2014**, *136* (14), 5460.

(11) Hawecker, J.; Lehn, J.-M.; Ziessel, R. *J. Chem. Soc., Chem. Commun.* **1984**, 328.

(12) Clark, M. L.; Cheung, P. L.; Lessio, M.; Carter, E. A.; Kubiak, C. P. *ACS Catal.* **2018**, *8* (3), 2021.

(13) Delis, J. G. P.; Chirik, P. J.; Tondreau, A. M. Hydrosilylation Catalysts. US 2011/0009565A1, 2011.

(14) Becke, A. D. *J. Chem. Phys.* **1993**, *98* (7), 5648.

(15) Tulyathan, B.; Geiger, W. E. *J. Am. Chem. Soc.* **1985**, *107* (21), 5960.

(16) Little, E. J.; Jones, M. M. *J. Chem. Educ.* **1960**, *37* (5), 231.

(17) Matsubara, Y. *ACS Energy Lett.* **2017**, *2* (8), 1886.

(18) Nicholson, R. S.; Shain, I. *Anal. Chem.* **1964**, *36* (4), 706.

(19) Saveant, J. M. *Electrochim. Acta* **1967**, *12* (7), 753.

(20) Hawley, M. D.; Feldberg, S. W. *J. Phys. Chem.* **1966**, *70* (11), 3459.

(21) Rieger, P. H. *Electrochemistry*, 2nd Editio.; Springer Netherlands: Dordrecht, 1994.

(22) Savéant, J.-M. *Elements of Molecular and Biomolecular Electrochemistry*; John Wiley & Sons, Inc.: Hoboken, NJ, USA, 2006.

(23) Connelly, N. G.; Geiger, W. E. *Chem. Rev.* **1996**, *96* (2), 877.

(24) Kochi, J. K. *J. Organomet. Chem.* **1986**, *300* (1–2), 139.

(25) Astruc, D. *Angew. Chem., Int. Ed.* **1988**, *27* (5), 643.

(26) Grice, K. A.; Gu, N. X.; Sampson, M. D.; Kubiak, C. P. *Dalton Trans.* **2013**, *42* (23), 8498.

(27) Wrighton, M. *Chem. Rev.* **1974**, *74* (4), 401.

(28) Fernández, S.; Franco, F.; Casadevall, C.; Martin-Diaconescu, V.; Luis, J. M.; Lloret-Fillol, J. *J. Am. Chem. Soc.* **2020**, *142* (1), 120.

(29) Cometto, C.; Chen, L.; Lo, P.-K.; Guo, Z.; Lau, K.-C.; Anxolabéhère-Mallart, E.; Fave, C.; Lau, T.-C.; Robert, M. *ACS Catal.* **2018**, *8* (4), 3411.

(30) Costentin, C.; Drouet, S.; Robert, M.; Savéant, J.-M. *Science* **2012**, *338* (6103), 90.

(31) Azcarate, I.; Costentin, C.; Robert, M.; Savéant, J.-M. *J. Am. Chem. Soc.* **2016**, *138* (51), 16639.

(32) Sampson, M. D.; Kubiak, C. P. *J. Am. Chem. Soc.* **2016**, *138* (4), 1386.

(33) Johnson, B. A.; Maji, S.; Agarwala, H.; White, T. A.; Mijangos, E.; Ott, S. *Angew. Chem., Int. Ed.* **2016**, *55* (5), 1825.

(34) Ngo, K. T.; McKinnon, M.; Mahanti, B.; Narayanan, R.; Grills, D. C.; Ertem, M. Z.; Rochford, J. *J. Am. Chem. Soc.* **2017**, *139* (7), 2604.

(35) Sung, S.; Li, X.; Wolf, L. M.; Meeder, J. R.; Bhuvanesh, N. S.; Grice, K. A.; Panetier, J. A.; Nippe, M. *J. Am. Chem. Soc.* **2019**, *141* (16), 6569.

(36) Zimmer, P.; Müller, P.; Burkhardt, L.; Schepper, R.; Neuba, A.; Steube, J.; Dietrich, F.; Flörke, U.; Mangold, S.; Gerhards, M.; Bauer, M. *Eur. J. Inorg. Chem.* **2017**, *2017* (11), 1504.